Earth and Planetary Science Letters 535 (2020) 116121

Contents lists available at ScienceDirect

Earth and Planetary Science Letters

www.elsevier.com/locate/epsl

Do sea level variations influence mid-ocean ridge magma supply? A test using crustal thickness and bathymetry data from the East Pacific Rise

Bridgit Boulahanis [a,*], Suzanne M. Carbotte [a], Peter J. Huybers [b], Mladen R. Nedimović [c], Omid Aghaei [c,1], Juan Pablo Canales [d], Charles H. Langmuir [b]

[a] Lamont-Doherty Earth Observatory of Columbia University, Palisades, NY 10964, USA
[b] Department of Earth and Planetary Sciences, Harvard University, Cambridge, MA 02138, USA
[c] Department of Earth Sciences, Dalhousie University, Halifax, Nova Scotia B3H 4J1, Canada
[d] Woods Hole Oceanographic Institution, Woods Hole, MA 02543, USA

ARTICLE INFO

Article history:
Received 9 May 2019
Received in revised form 23 December 2019
Accepted 24 January 2020
Available online 10 February 2020
Editor: R. Bendick

Keywords:
mid-ocean ridges
glacial cycles
crustal thickness
East Pacific Rise
multi-channel seismic
magmatism

ABSTRACT

Recent studies suggest that eustatic sea level fluctuations induced by glacial cycles in the Pleistocene influence mantle-melting and volcanic eruptions at mid-ocean ridges, with models predicting variations in oceanic crustal thickness and seafloor bathymetry linked to sea level change. Analyses of seafloor bathymetry have found evidence of significant spectral energy at frequencies consistent with Milanković cycles of 1/23, 1/41, and 1/80-1/120 ka^{-1}. However, other studies emphasize the need for crustal thickness observations to test the "sea level hypothesis".

Here we investigate the hypothesis of climate driven periodicity in mid-ocean ridge magmatism through analysis of a unique bathymetry and crustal thickness dataset derived from a 3D multi-channel seismic investigation of the East Pacific Rise from 9°42' to 57'N. Crustal thickness data spans the last ~235 ka in age and reveals three axis-parallel zones of 200-800 m thicker crust. The amplitude and spacing of these thick crust ridges, which are most prominent on the east flank of the ridge, are consistent with predictions of sea level modulated mantle melting. Similarly spaced ridges are apparent in the longer duration (470 ka) seafloor bathymetry data. Spectral analysis of these datasets shows peaks centered near 1/80 ka^{-1} and locally near 1/41 ka^{-1} on the east flank in both bathymetry and crustal thickness. West flank spectral results show intermittent peaks near 1/100 ka^{-1} and 1/41 ka^{-1} in crustal thickness and no coherent peak frequencies in bathymetry data. We attribute differences between the east and west flank to the impacts of spatially variable asymmetric spreading and small changes in the locus of accretion. Observed half spreading rates are dominantly faster to the east with small ridge jumps transferring crust from the west flank. Lagged cross-correlations between sea level and crustal thickness indicate a maximum when the latter is lagged by ~45 ka, which align thick crust zones with the ~100 ka periods of lower sea level. Crustal thickness is also directly compared with seafloor bathymetry, indicating a component of compensated topography with RMS relief at the seafloor of 10 to 29% of crustal thickness variations. However, complexity inherited from variable asymmetric spreading and seafloor faulting is also apparent, and results provide new insights into how the crustal accretion filter modulates the recording of magma supply variations in the crust and in seafloor relief.

While the significance of the statistical analysis of these ridge records is limited by the short duration of the available crustal thickness dataset and effects of asymmetric spreading, the novel observations of crustal thickness varying at timescales of ~80-100 ka require a mechanism, and the sea level hypothesis provides a plausible explanation.

* Corresponding author.
E-mail address: BridgitB@ldeo.columbia.edu (B. Boulahanis).
[1] Present address: Ocean Networks Canada, Victoria, BC, Canada.

https://doi.org/10.1016/j.epsl.2020.116121
0012-821X/

1. Introduction

The abyssal hills that cover the deep ocean floor are the most common morphologic features on earth's surface (e.g. Macdonald et al., 1996). These structures form at Mid-Ocean Ridges (MORs) and correspond with relatively regularly spaced ∼1 to 10 km wide fault-bounded bathymetric highs and lows oriented parallel to the ridge axis (e.g. Macdonald, 1982; Goff and Jordan, 1988). Models of abyssal hill formation fall into two end member groups: those that invoke primarily extensional faulting linked to seafloor spreading versus those that suggest magmatic cycles related to fluctuations in mantle melt supply (e.g. Kappel and Ryan, 1986; Carbotte and Macdonald, 1994; Macdonald, 1998; Buck et al., 2005). Extensional faulting models are generally favored. However, recent studies have led to renewed debate concerning the origin of these features, suggesting that variations in melt supply to MORs due to glacially modulated fluctuations in sea level contribute to abyssal hill relief (Huybers and Langmuir, 2009; Lund and Asimow, 2011; Crowley et al., 2015). A related hypothesis is that both direct orbital forcing and sea level change may contribute to the frequency of seafloor eruptions, which generate the extrusive layer of oceanic crust and contribute to abyssal hill topography (Tolstoy, 2015).

Glacial-interglacial cycles during the Pleistocene account for a transfer of 5×10^{19} kg of water between continental ice sheets and the ocean, leading to eustatic sea level variations on the order of 100 m (e.g. Tushingham and Peltier, 1991). Models of mantle melting beneath MOR predict that changes in lithostatic pressure associated with sea level rise and fall of this magnitude will result in variations in decompression melting in the mantle of ±10% (Crowley et al., 2015). The effect of sea level variations on MOR magmatic systems could lead to variations in hydrothermal metal fluxes (Lund and Asimow, 2011; Lund et al., 2016; Middleton et al., 2016; Costa et al., 2017), ridge CO_2 emissions (Burley and Katz, 2015; Tolstoy, 2015; Huybers and Langmuir, 2009; 2017; Cerpa et al., 2019), frequency of seafloor eruptions (Tolstoy, 2015; Lund et al., 2018), and oceanic crustal thickness (Crowley et al., 2015). If variations in crustal thickness contribute to abyssal hill topography through isostatic or flexural compensation then temporal modulations in mantle melt supply to the crust may be expressed in the width and height of abyssal hills.

As a test of the proposed relationship between glacial cycles and abyssal hill topography, Crowley et al. (2015) employed spectral analysis of bathymetry records from a portion of the Australian-Antarctic Ridge and found that abyssal hill topography is periodic at the Milanković frequencies associated with sea level variations of ∼1/100 ka^{-1}, 1/41 ka^{-1}, and 1/23 ka^{-1}. Tolstoy (2015) analyzed bathymetry from the southern East Pacific Rise (EPR) and found evidence for periodic variations at 1/100 ka^{-1}.

Other studies, based on numerical models of MOR faulting as well as statistical characterization of abyssal hill relief, conclude that the periodic signals detected in recent spectral studies are more likely to reflect fault-growth processes rather than temporal fluctuations in mantle melt supply (Olive et al., 2015; Goff, 2015). Olive et al. (2015) present a simple tectono-magmatic model of abyssal hill formation by faulting that predicts changes in dominant fault spacing with spreading rate, that are broadly consistent with prior observations of abyssal hill characteristics. A recent global-scale study showed that averaging seafloor bathymetry over large regional areas as a function of crustal age in order to suppress expected random variability (e.g. due to faulting and seafloor volcanism) shows no statistically significant indication of climate driven variations in bathymetry (Goff et al., 2018).

A number of crustal emplacement processes are expected to act as a low-pass filter on how the flux of magma from the mantle is recorded in crustal properties. These include volcanic eruptions, where lava flows can extend 1 km or more from the axis (e.g. Soule et al., 2007), and the damping effects of the 4-6 km wide magma storage zone within the lower crust inferred from seismic studies (Dunn et al., 2000; Canales et al., 2012). Olive et al. (2015) suggest that volcanic eruptions and faulting contribute most directly to seafloor relief and will effectively overprint any temporal fluctuations in mantle melt supply, making the influence of Milanković-period variations, if they exist, undetectable in seafloor bathymetry.

Oceanic crustal thickness provides a direct measure of magma flux to the crust over the width of the active accretion zone. At fast spreading ridges, predicted crustal thickness variations due to sea level modulated mantle melt supply (on the scale of hundreds of meters) are an order of magnitude larger than the typical seafloor relief (tens of meters) and should be readily detectable in crustal thickness records of sufficient resolution. Further, the effects of seafloor faulting and volcanic overprint that dominate abyssal hill topography will have less impact on crustal thickness records. Hence, analysis of crustal thickness provides arguably the best and most direct test of the hypothesis that production of oceanic crust is modulated by glacially driven sea level variations. In this study, we utilize a unique high-resolution crustal thickness and bathymetry data set from the fast spreading northern EPR derived from 3D multi-channel seismic imaging in order to investigate the sea level hypothesis. This dataset provides a near complete image of the base of the crust to ages of 235 ka on average, and reveals three ridge-parallel zones of thicker crust spaced ∼80 ka apart. Co-located high-resolution bathymetry data are available to crustal ages of ∼470 ka and reveal lineated ridges of similar spacing. We utilize spectral analysis, cross-correlations, and evaluation of root-mean square relief to further characterize the variability in these datasets, examine correlations between crustal thickness and sea level records, and evaluate the relationship between crustal thickness and bathymetry.

2. Study area

Our study is centered on the EPR from 9°42′N to 9°57′N (Fig. 1) where the Cocos and Pacific places are spreading apart at a half rate of ∼55 mm/yr (Carbotte and Macdonald, 1992). The region crosses the youngest of the Lamont Seamounts (Sasha seamount) in the northwest and a portion of the volcanic flow field associated with the Watchstander seamounts in the northeast (Fornari et al., 1998; Macdonald, 1982). Off-axis melt bodies in the crust have been detected in the region on both ridge flanks (Canales et al., 2012). Three previously identified fine-scale discontinuities are located along the ridge axis centered at ∼9°44′N 9°48-49′N and 9°51.5′N with a fourth extending beyond the northern end of our study region from 9°56′-58′N (Haymon et al., 1991; White et al., 2002; 2006; Haymon and White, 2004; Carbotte et al., 2013). Seismic imaging shows disruptions in the mid-crust axial magma lens (Carbotte et al., 2013) and local zones of lower and higher melt content in the uppermost mantle melt reservoir (Toomey et al., 2007) from which along-axis segmentation of the modern day magmatic system from crust to upper mantle is inferred (Marjanović et al., 2018).

Previous studies of crustal thickness in the region include a 2D study conducted in the 1980s that revealed small variations (few 100 m) in crustal thickness along crustal flow-lines, from which near steady-state accretion was inferred (Barth and Mutter, 1996). A later regional tomography study was conducted which revealed long-wavelength crustal thickness variations over tens of kilometers primarily in the ridge-parallel direction (Canales et al., 2003). In 2008 a 3D multi-channel seismic (MCS) study was conducted, providing the highest resolution image of the base of the crust of anywhere in the global oceans (Aghaei et al., 2014). For their study, Aghaei et al. (2014) used post-stack time migration (Post-STM)

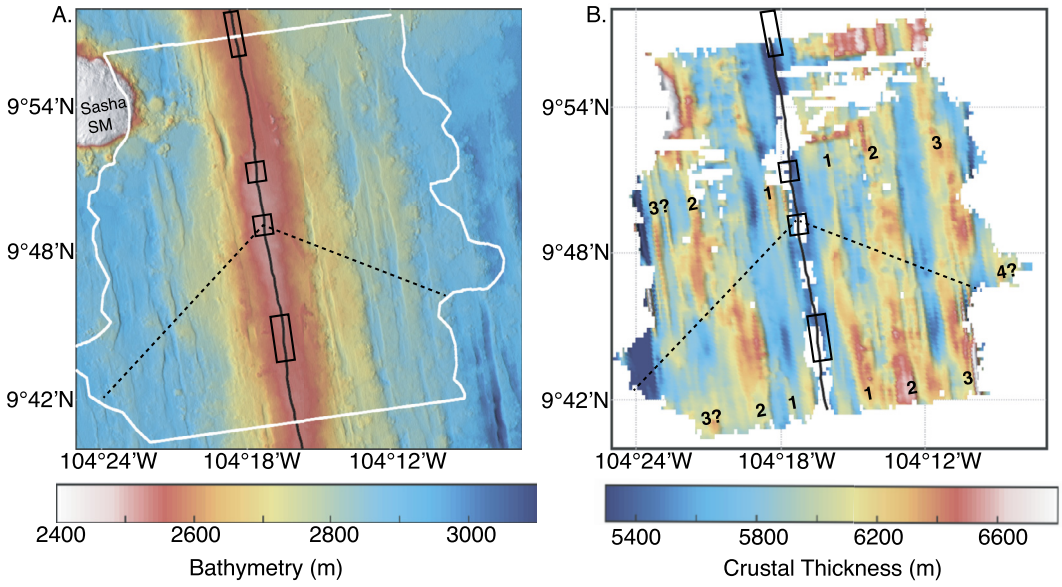

Fig. 1. Seafloor bathymetry and crustal thickness data from the East Pacific Rise. A. Bathymetry with outline of region of crustal thickness data superimposed (white line). Sasha Seamount, located in the northwest corner of the study region, is indicated. Note that the bathymetry data used in analysis extends beyond the region shown to ~25 km from the ridge axis (Fig. 2). B. Map of crustal thickness from Aghaei (2013). Numbers indicate thick crust regions (TCRs). Also shown is location of ridge axis (solid black line), previously identified ridge-axis discontinuities (black boxes), and interpreted trace of long-lived discontinuity (dashed black lines).

imaging and were able to identify Moho in 87% of the imaged volume in contrast to the intermittent Moho imaged in prior 2D studies in the region (Supplemental text 1).

3. Crustal thickness and bathymetry data

The data used for the current study were derived from the same 3D MCS investigation but using crustal thickness derived from more advanced analysis using 3D Kirchhoff pre-stack time migration (Pre-STM) (Aghaei, 2013) which yields more accurate imaging in regions of complex structure. The input to the Pre-STM was the full 3D data set with the output grid of 6.25 m in the cross-axis direction and 300 m in the along-axis direction. The Pre-STM provides further improvement in imaging over the earlier Post-STM results with Moho identified in 92% of the imaged volume. However, the more significant advantage over the prior study is for the crustal thickness estimation derived from the Moho picks, which makes use of the detailed 3D velocity model obtained from Pre-STM to convert crustal travel-times to crustal thickness. This velocity model is obtained directly from the MCS dataset using the migration velocity analysis method and exploits the high MCS data density to provide a much more accurate model than the 2D OBS-derived model used in the Aghaei et al. (2014) study (Supplemental text 1).

In addition to the crustal thickness data set, we also examine a coincident 25 m grid interval bathymetry dataset derived from the same experiment. This dataset is of higher resolution than the prior bathymetry data available for the region and is derived by gridding the multiple passes of redundant coverage multi-beam swath sonar data acquired continuously during the MCS survey.

3.1. Observations

Crustal thickness data reveal a series of lineated, ridge-parallel zones of alternating thicker and thinner crust that extend for much of the study area (Fig. 1B). On the east flank of the EPR, three prominent Thick Crust Regions (TCRs) of 200-800 m thicker crust are present, each ~2-3 km wide (Fig. 1B). Where crustal thickness data extends farthest from the ridge axis there is evidence of a fourth band of thicker crust measuring at least 2 km wide (centered at ~9°47′N).

On the west flank, three TCRs can also be identified but 2 of the 3 are more intermittent than those on the east flank (Fig. 1B). TCR 1 is located closer to the modern ridge axis with less along-axis continuity than its east flank counterpart and is narrower (~1.5 km wide). The second west flank TCR is ~4 km wide and up to 800 m thicker than adjoining crust. TCR 3 is intermittently identified south of Sasha Seamount, and corresponds with a narrow (~0.5 km) band of ~200 m thicker crust than the surrounding region.

On both ridge flanks the along-axis continuity of the three TCR are interrupted, defining a v-shaped zone of offset ridges that is centered about the ridge axis at ~9°49′N. This location coincides with one of the small discontinuities in the modern axial zone and in the crustal magmatic system below (Fig. 1). The presence of this ridge flank discontinuity zone indicates this small ridge offset has persisted in the region, migrating north along the ridge axis through time.

Seafloor bathymetry in the region is typical of magmatically robust regions of fast spreading crust and shows numerous ridge-parallel faults with offsets of tens of meters. A prominent ~3 km wide axis-parallel ridge is also evident on the east flank extending north of ~9°44′N (Fig. 1A). In order to better highlight the intermediate scale variations in bathymetry on these length scales, we remove the long wavelength trends associated with the shallow axial high and seafloor subsidence (Fig. 2).

Filtered bathymetry indicates ridge parallel bands of shallower and deeper seafloor of similar widths as the TCRs. On the east flank, we identify 6 regions of shallow seafloor over the 25 km extent of our data, with peaks rising 20-60 m above average depths and widths of ~2 km. Much like TCR observations, bathymetry ridges are more laterally continuous on the east flank than on the west. West flank bathymetry shows 5 regions of shallow seafloor, with similar amplitudes but more variable widths (ranging 1-4 km) than on the east flank.

3.2. Conversion to crustal age

In order to assess the timescale of the quasi-periodic variations apparent in bathymetry and crustal thickness data, as well

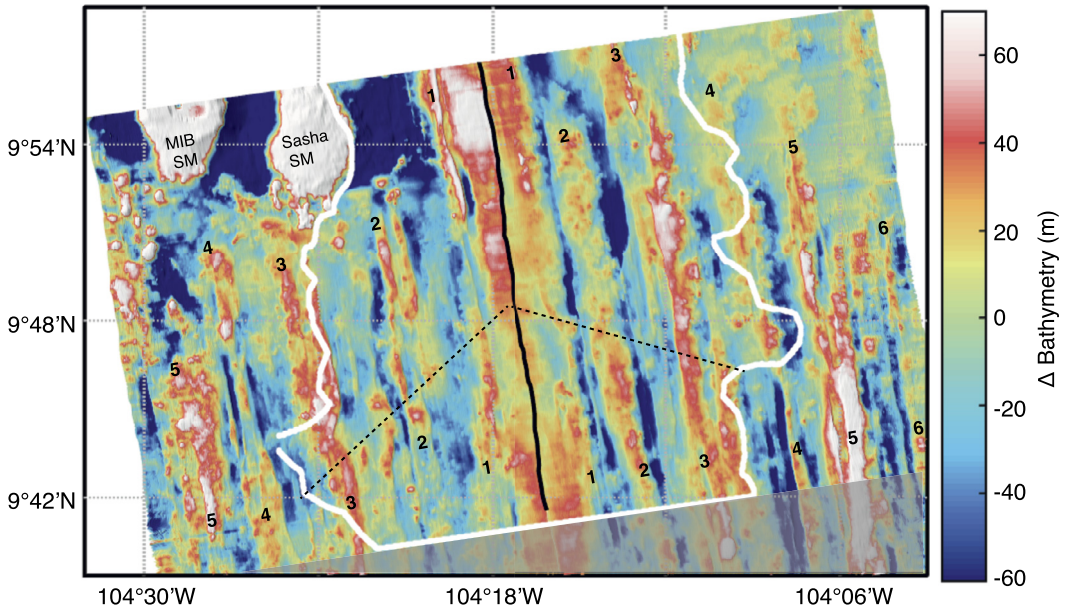

Fig. 2. Filtered seafloor bathymetry. Residual bathymetry filtered to remove long wavelength trends and highlight intermediate wavelength topography (pass band 75 m to 6.25 km). Numbers indicate interpreted intermediate-scale ridges of shallower bathymetry. Sasha Seamount and MIB Seamount are labeled; greyed region in south indicates data not included in analysis. Other annotation as in Fig. 1.

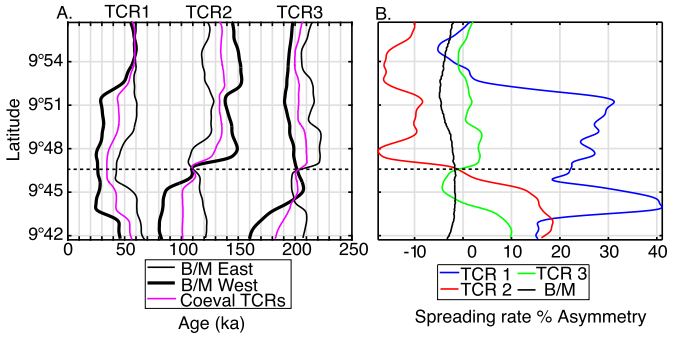

Fig. 3. Age models, half spreading rate, and percent asymmetry. A. Ages of crustal thickness peaks at each TCR (for full TCR peak locations, see Fig. S2A) calculated using the coeval TCR age model (magenta) and the Brunhes-Matuyama (B/M) based model for the west flank (bold black) and east flank (narrow black) of the ridge axis. Black dashed line is location of profile shown in Fig. 4. Using the B/M age model, ages of the conjugate TCRs differ for each ridge flank, suggesting substantial asymmetric spreading that is not accounted for using the spreading rate determined for the duration of the Brunhes period (see section 3.2). B. Percent spreading rate asymmetry determined from TCR age model compared with asymmetry calculated from the Brunhes-Matuyama reversal. Colors as in legend. Asymmetry is calculated as the percent difference between half spreading rates (for TCRs 1, 2, 3 and the B/M) and the mean half spreading rate along each profile (~53 mm/yr), with positive values indicating a faster half spreading rate for the east flank. Average percent differences between half spreading rates are 19%, 13%, 3%, and 3% for TCRs 1, 2, 3, and the B/M respectively. (For interpretation of the colors in the figure(s), the reader is referred to the web version of this article.)

as to explore the potential relationship with the history of global sea level, the datasets are converted to crustal age. An age model is constructed, first using the location of the Brunhes-Matuyama (B/M) magnetic reversal at 780 ka (from Carbotte and Macdonald, 1992, Fig. S1). Utilizing this age model yields significantly different ages for TCRs across the two ridge flanks, suggesting asymmetric spreading that is not accounted for using spreading rates determined for the duration of the Brunhes period (Fig. 3A). In order to account for this asymmetric accretion, we generate a new age model assuming that conjugate TCRs on the two ridge flanks are coeval. We estimate ages along each TCR by identifying the peak in crustal thickness along each TCR (Fig. S2A), measuring the distance between conjugate TCR peaks along profiles oriented perpendicular to the ridge axis, and converting to age using the full spreading rate determined from the B/M reversal. This analysis yields average ages of 48 ± 9, 124± 15, and 202 ± 16 ka for TCRs peaks 1-3 respectively (Fig. 3A), indicating an average spacing of 77 ka. Average ages of the bathymetric ridges identified beyond the extent of our crustal thickness dataset are 306 ± 29, 371 ± 23, and 445 ± 4 (east flank only) respectively, yielding an average spacing of 80 ka over the 470 ka duration.

Comparing the TCR ages generated using the B/M reversal with those assuming coeval TCRs provides a measure of average temporal uncertainties of 9 ± 2 ka in crustal ages (Fig. 3A), which we attribute to variable asymmetric spreading. Half spreading rates calculated from the coeval TCR model indicate average differences of 20, 13, and 3 mm/yr for TCRs 1, 2, and 3 respectively, with spreading on the east flank generally faster than the west (Fig. S2B). The amount and sense of spreading asymmetry also varies spatially along the ridge axis, with step-wise shifts broadly consistent with the ridge segmentation (Fig. 3B). It is likely that small (hundreds of meters to kilometer-scale) jumps in the locus of accretion within individual spreading segments contribute to the variable spreading asymmetry we infer in the study area. The zone of active crustal formation, as indicated by anomalously thin crust surrounding the ridge axis, is on average ~1.5 km wide in our study area (Fig. 1B). Small ridge jumps of ~0.5 km equivalent to the estimated average temporal uncertainty of 9 ± 2 ka would be readily accommodated within this crustal accretion zone.

Given the significant evidence for variable asymmetric accretion we favor the coeval TCR age model and use this model for comparisons with the history of relative sea level (RSL) variations. Analyses using the age model determined using the B/M reversal only are also provided in the supplemental material (Figs. S3-S5) for comparison.

3.3. Comparison with relative sea level

We compare bathymetry and crustal thickness records with the RSL curve of Grant et al. (2014), which provides a high-resolution record of sea level variations over the last 500 ka. RSL is observed to vary at periodicities of ~1/23 ka^{-1}, 1/41 ka^{-1} and between 1/80 ka^{-1} and 1/120 ka^{-1} (e.g. Raymo, 1997). Variations in

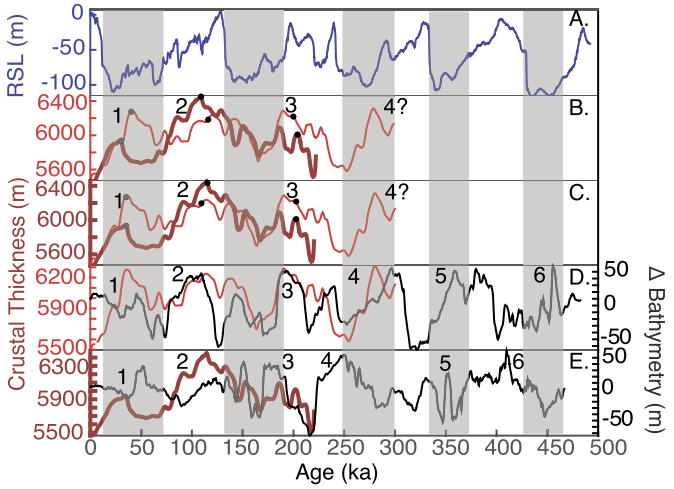

Fig. 4. Time series comparison of relative sea level (RSL), crustal thickness, and bathymetry. A. RSL (blue) from Grant et al. (2014), with grey bars indicating low RSL (glacial) periods as indicated by even Marine Isotope Stages. B. Example crustal thickness profile taken from period of longest data (see Fig. 3) after converting to crustal age using the Brunhes-Matuyama (B/M) regional magnetics model (see Section 3.3) with the east flank in red and west flank in maroon. This model results in age offsets between conjugate TCRs on the two flanks, particularly TCR1. C. Example crustal thickness profile as in B, but converted to crustal age using coeval TCR age model. East flank (red) and west flank (maroon) TCRs are better aligned with this model, with the location of peak TCRs indicated by black dots. D. East flank crustal thickness (red) and residual bathymetry (black), converted to age using the coeval TCR age model. On the east flank crustal thickness and bathymetry appear to covary, with periods of thick crust associated with shallow bathymetry. E. West flank crustal thickness (maroon) and residual bathymetry (black). On the west flank bathymetry and crustal thickness are less well aligned than the east, with little indication that the two are covarying. Black numbers indicate interpreted locations of crustal thickness and bathymetry ridges as in Figs. 1B and 2.

bathymetry and crustal thickness on the timescale of ~80 ka are therefore roughly of the same wavelength as long period ice age cycles evident in the RSL record.

Comparing an example profile taken from our region of longest crustal thickness data with RSL (Fig. 4) indicates that two of three TCRs are roughly aligned with sea level highs and one with a low sea level period. East flank TCRs are of comparable widths and spacing to glacial cycles, as is TCR 2 on the west flank, but west flank TCRs 1 and 2 are narrower though comparably spaced. Bathymetry ridges are generally narrower than either glacial cycles or TCRs on both flanks. Shallow bathymetry regions 4 and 5 align with a transition from low to high RSL, while ridge 6 peaks in a period of low sea level. While bathymetry and crustal thickness ridges align in some places, there is significant misalignment in others. Comparison profiles for the entire study area are provided in supplemental figures S6 and S7.

4. Statistical analyses of crustal thickness, bathymetry and correlations with relative sea level

4.1. Methods

In order to examine regional variability profiles are extracted perpendicular to the ridge axis every 150 m along axis from the bathymetry data and every 300 m along axis from the crustal thickness data. Crustal thickness profiles extend up to a maximum of 16 km from the ridge axis corresponding to crustal ages of 310 ka, with an average profile length of 12.5 km (235 ka). Our high-resolution bathymetric data coverage extends further from the ridge axis to 25 km (~470 ka). Prior to analyses we remove data from the presumed zone of active accretion, where MOR crust is still in the process of forming. In bathymetry, we exclude the shallow axial high, demarcated here as the region shallower than 2650 m. In crustal thickness data we exclude the zone of anomalously thin crust and intermittent Moho imaging bounding the ridge axis (crustal thickness values $\leq$ 5600 m, Fig. 1B). Prior to analysis, bathymetry data are also detrended by subtracting the square root of age in order to remove long-term trends associated with seafloor subsidence as newly formed lithosphere cools (e.g. Parsons and Sclater, 1977).

Spectral analysis is undertaken using a windowed periodogram with a single discrete prolate spheroidal sequences taper (e.g. Percival and Walden, 1993). This approach is equivalent to the multitaper method used in Crowley et al. (2015) but with use of a single taper due to the short duration of our time series. The data are prepared for spectral analysis by prewhitening, taking the first derivative of the data in order to reduce the slope of the background continuum, facilitating the identification of spectral peaks (Crowley et al., 2015). There are a number of factors that contribute to frequency resolution and need to be considered in the interpretation of results. These include the dataset sampling interval, temporal uncertainties in the crustal age model, and the length/duration of the available data.

The nominal spatial resolutions of both the crustal thickness (6.25 m and 37.5 m respectively in the ridge-normal direction) and bathymetry datasets should be adequate for resolving the range of Milanković cycles. However, the practical spatial resolution of the crustal thickness dataset will be much less than the nominal resolution given that the pre-stack velocity analysis used to derive crustal thickness from crustal travel times is conducted on a coarser interval and making use of neighboring common image gathers up to 1 km away (Aghaei, 2013). Based on this consideration, we conservatively do not interpret frequencies higher than 1/27 ka^{-1} (spatially < 1.5 km, Supplemental text 2) in crustal thickness spectra.

In addition to issues of spatial resolution, uncertainty in the age model used to convert from distance to crustal age may impact results of spectral analysis. Temporal uncertainties estimated from comparison of Brunhes-Matuyama and coeval TCR ages are of order of $\pm$10 ka and are not uniform across the study area. Previous studies have shown how frequencies shorter than ~1/100 ka^{-1} may be difficult to detect with a temporal "jitter" of this magnitude (e.g. Huybers and Wunsch, 2004).

The ability of spectral analysis to resolve frequencies of interest also depends on the duration of the time series available; at the lowest-resolved frequencies and using a minimum number of tapers, data spanning at least three cycles are needed for purposes of distinguishing between peaks and background variability (Percival and Walden, 1993). Given this constraint we expect the ~500 ka duration of our bathymetry dataset will be adequate to resolve Milanković periods of interest but the shorter crustal thickness dataset may be inadequate to resolve the longest ice age cycles with timescales of ~100 ka. To illustrate how the limited length of our dataset influences resolvable frequencies, we compute spectral estimates for varying durations of the sea level record. Results of spectral analysis of the RSL record, after limiting to ages of 200 to 500 ka (Fig. 5), show maximum spectral power near Milanković frequencies at all dataset lengths. At lengths of less than 300 ka (comparable to our crustal thickness dataset), frequencies within the precession (1/22 - 1/25 ka^{-1}) and obliquity (1/37 and 1/44 ka^{-1}) bands are well resolved, and a broad weak band of power is observed between 1/77 and 1/143 ka^{-1} which spans but is wider than the band of 1/80 to 1/120 ka^{-1} generally observed in climate records. There is also a band of weak power outside of Milanković frequencies centered at 1/65 ka^{-1} in spectra of profiles up to 425 ka in length. At lengths of 450 ka and greater (comparable to bathymetry data extent), spectral peaks become sharper and narrower with power at the longest frequencies more clearly focused from 1/83 ka to 1/112 ka^{-1}. These results show

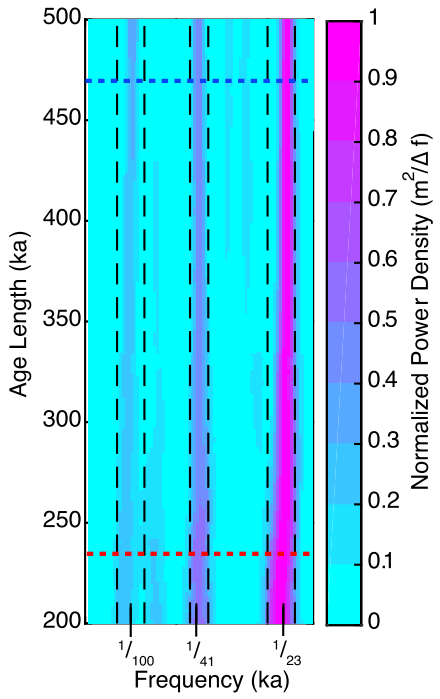

Fig. 5. Spectral analysis of the relative sea level record at increasing dataset lengths. Analysis on the Grant et al. (2014) RSL record is undertaken using the multitaper method with a single taper. Spectral power is normalized between 0 and 1 and shown in terms of frequency and dataset length (ka), with spectral power indicated by color. The red dashed line indicates the average crustal thickness dataset length (235 ka), the blue dashed line the average bathymetry dataset length (470 ka). Vertical black dashed lines indicate frequencies surrounding Milanković frequency bands where spectral power is increased at dataset lengths comparable to average crustal thickness profile length: surrounding the precession band between 1/22 and 1/25 ka^{-1}, the obliquity band between 1/37 and 1/44 ka^{-1}, and between 1/77 and 1/143 ka^{-1} which spans but is wider than the eccentricity band of 1/80 to 1/120 ka^{-1} (e.g. Raymo, 1997). The distribution of spectral power near Milanković frequencies show how the limited length of our time series smears spectral peaks into broader regions, and provides a framework for interpreting spectral power in crustal thickness (Fig. 6) and bathymetry (Fig. 7).

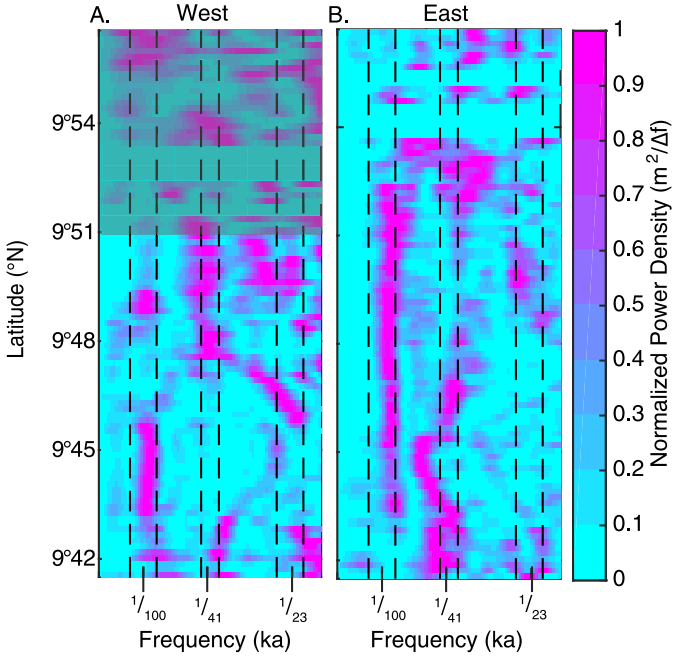

Fig. 6. Normalized crustal thickness spectrograms. Spectrograms of western (A) and eastern flank (B) crustal thickness calculated using the multitaper method with a single taper on profiles extracted from full crustal thickness grids (Fig. 1B) after prewhitening (see Methods, 4.1) are shown plotted by latitude of the ridge axis crossing on each profile, with warmer colors indicating greater spectral energy. Black dashed lines indicate frequencies of increased power surrounding Milanković cycles as in Fig. 5. The grey shaded region on the west flank indicates the area in which the anomalously thick crust and shallow bathymetry in the area of Sasha Seamount overprints MOR generated crust.

how the limited length of our time series smears spectral peaks into broader regions of power (and weaker for the ~1/100 ka^{-1} band), and provides a framework for interpreting spectral power in crustal thickness and bathymetry results.

The relationships between RSL and crustal thickness are further explored using lagged cross-correlation analysis. We do not conduct coherence analysis between crustal thickness and RSL as it generally requires twice the tapers as multitaper spectral analysis (Percival and Walden, 1993), and a longer time series would be a requirement for assessing coherence. Profiles are filtered to frequencies between 1/10 ka^{-1} and 1/150 ka^{-1} to remove the presence of high frequency noise and long-term trends outside our frequencies of interest. Cross-correlations are calculated between RSL and crustal thickness profiles to determine the time offset, or lag, of best correlation. Correlations are calculated only in the direction of RSL change occurring prior to crustal thickness variation, and so lags in this analysis are positive in sign. Correlation results are plotted by latitude of the ridge axis intersection along each profile (Figs. 8 A&B). Example stacked profiles are plotted for each ridge flank bounding the regions where the highest correlations are observed with the calculated optimal time lag applied (Fig. 8C).

Cross-correlations are also calculated between crustal thickness and bathymetry datasets following the same methods in term of distance from the ridge axis rather than time (Figs. 9 A&B). Correlations are calculated in this case with positive lags indicating crustal thickness profiles are shifted to further from the ridge axis and negative indicating crustal thickness shifted closer to the ridge axis to match bathymetry. Maximum and mean correlation coefficients are reported as well as standard deviation (±). As a measure of the typical amplitude of variation in bathymetry and crustal thickness, we calculate the root mean square (RMS) height and thickness (Fig. 9C). The calculated RMS amplitudes for bathymetry and crustal thickness correspond to the average variation from the mean depth and thickness respectively.

4.2. Results

4.2.1. Spectral analysis

Results of spectral analysis of crustal thickness data are shown in Fig. 6. Crustal thickness spectra for the west flank indicate intermittent power centered at 1/100 ka^{-1} (spanning 1/77 – 1/125 ka^{-1}, Fig. 6A). From 9°47′N to 9°51′N power is centered at 1/44 ka^{-1} and north of 9°51′N is broadly distributed. Crustal thickness spectra on the east flank show power focused along two main bands (Fig. 6B). In the south, from 9°42′N to 9°47′N power is centered between 1/36 ka^{-1} and 1/63 ka^{-1}. Increased spectral power is observed on the east flank from 9°43′N to 9°52′N centered at 1/83 ka^{-1} (spanning 1/67 to 1/125 ka^{-1}). North of 9°52′N power is intermittent.

West flank bathymetry spectra show little evidence of consistent frequencies of increased spectral power except at the northern end of our study area, where Sasha seamount dominates topography (Fig. 7A). East flank bathymetry spectra show increased spectral power south of 9°48′N spanning 1/30 to 1/50 ka^{-1}, centered at ~1/41 ka^{-1} (Fig. 7B). North of 9°48′N power shifts to be centered at 1/77 ka^{-1} (spanning 1/66 to 1/90 ka^{-1}). Intermittent power is observed throughout bathymetry spectra from both flanks, with regions displaying increased power at ~1/25 ka^{-1}.

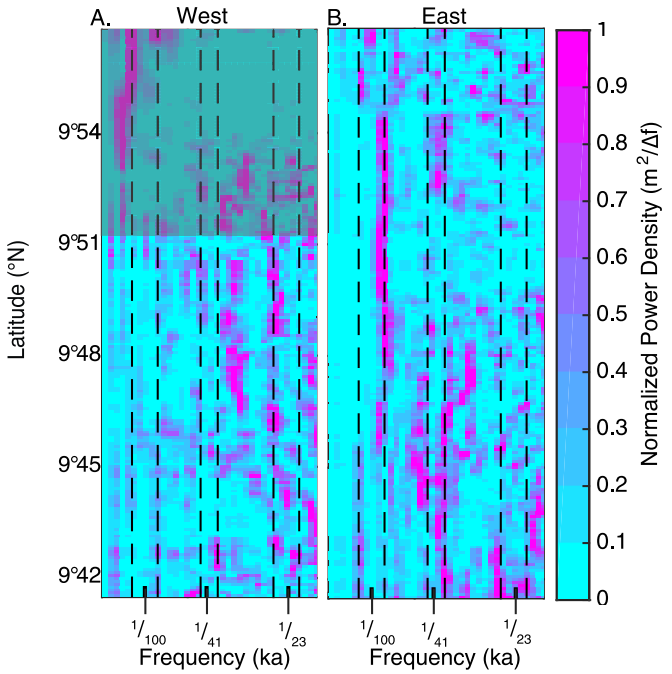

Fig. 7. Normalized bathymetry spectrograms. Spectrograms of western (A) and eastern flank (B) bathymetry calculated as for crustal thickness (Fig. 6) for profiles extracted from full bathymetry grid to average crustal ages of 470 ka (Figs. 1A & 2) and plotted by latitude of the ridge axis crossing on each profile. Annotated as in Fig. 6.

4.2.2. Correlations between crustal thickness and RSL

Cross correlations between crustal thickness and RSL are variable but show good correlations at a dominant time lag of ∼45 ka across much of the study region. The average lag of maximum correlation on the west flank is 46 ± 28 ka, with 66% of profiles displaying maximum correlations within that range (Fig. 8A). Average peak correlation coefficients on the west flank are 0.43 ± 0.17, with maximum correlation coefficients of 0.74. The average lag of maximum correlation on the east flank is 44 ± 16 ka, with 77% of profiles displaying maximum correlations within that range (Fig. 8B). Average east flank peak correlation coefficients are 0.36 ± 0.12 with maximum correlation coefficients of 0.60. Shifting example profiles from each flank to the regional lag of best correlation aligns the dominant periods of thicker crust with the ∼100 ka periods of lower RSL and thin crust during periods of high RSL (Fig. 8C).

4.2.3. Comparisons between crustal thickness and bathymetry records

Cross correlations calculated between crustal thickness and bathymetry indicate good correlations at lags near 0 offset for some of the study area, consistent with isostatic compensation. However, for much of the region maximum correlations are at non-zero offsets. West flank correlations between bathymetry and crustal thickness are variable along axis – good correlations are observed at an offset of approximately -2.25 km south of 9°45′N, with the negative lag indicating thickness data needs to be shifted to ridgeward to match bathymetry (Fig. 9A). Average west flank correlation coefficients are 0.55 ± 0.22, and maximum correlation coefficients are 0.95. The strongest east flank correlations are at a negative lag of ∼1.75 km found north of 9°46.5′N (Fig. 9B). Average east flank peak correlation coefficients are 0.55 ± 0.17 with maximum correlation coefficients of 0.88.

On the east flank, bathymetric RMS amplitudes average 39 ± 10 m and for the west flank south of Sasha seamount bathymetric RMS amplitudes average 54 ± 11 m (Fig. 9C). East and west flank crustal thickness RMS amplitudes average 210 ± 37 m and 221 ± 79 m respectively (Fig. 9D). On the east flank bathymetry RMS amplitudes average 19% of crustal thickness RMS amplitudes, whereas on the west flank bathymetry RMS amplitudes average 25% of crustal thickness RMS amplitudes.

5. Discussion

5.1. Testing the sea level hypothesis

The high-resolution crustal dataset used in this study reveals a series of ridge-parallel bands, ∼1.5-4 km in width, of alternating thicker and thinner crust (Fig. 1B, 2) particularly apparent on the east flank of the ridge axis. While the width and axis-parallel continuity of these thick/thin bands is less on the west flank, crustal thickness ridges of similar scale and periodicity as those on the east flank are observed. Temporal variations in mantle melt production and/or episodicity in melt delivery to the crust on short time intervals of ∼80 ka are indicated.

Simple models of depressurization mantle upwelling suggest sea level changes on the order of 100 m associated with the glacial cycles of the late Pleistocene could be associated with 10% changes in melt production, equivalent to 600 m for a 6 km average crustal thickness (Huybers and Langmuir, 2009; Lund and Asimow, 2011). More sophisticated mantle upwelling and melt transport models show the amplitude of the response depends on the frequency of the sea level forcing and spreading rate (Crowley et al., 2015; Burley and Katz, 2015). The variations in crustal thickness of 200-800 m found on both flanks in our study (Fig. 1B) are consistent with these model predictions. Further, spectral analysis of crustal thickness data confirms the presence of ∼1/80 ka^{-1} frequencies on the east flank and more intermittent ∼1/100 ka^{-1} power on the west (Fig. 6). These periods are comparable to the long wavelength ice age cycles of the late Pleistocene. Spectral analysis also indicates intermittent crustal thickness variations at the ∼1/41 ka^{-1} obliquity frequency, which are predicted by the numerical models of Crowley et al. (2015) at fast spreading ridges.

In prior studies, primarily using geochemical observations, where temporal variability in crustal accretion processes are inferred, melting events due to convective instabilities in the upper mantle or presence of melting anomalies due to the mantle heterogeneities have been invoked (e.g. Batiza et al., 1996; Regelous et al., 1999). These and other crustal level processes, such as off-axis volcanism and the lateral flow of erupted lavas, (e.g., Sims et al., 2003) may contribute to our observation of temporal variability in crustal production. However, the findings of quasi-periodic crustal thickness variations consistent with model predictions in both amplitude and frequency are a novel observation that point to sea level variations as a potential modulating force in crustal production in this region.

Results of cross-correlation analysis between crustal thickness and RSL (Fig. 8) provide further support for this hypothesis. In the Crowley et al. (2015) model, the generation of depressurization mantle melt anomalies is expected to be most sensitive to the rate of sea level change relative to the time required to deliver melt from depth to the surface. Cross-correlations calculated between crustal thickness and rate of sea level change (dRSL) are negligible, which may be attributed to the high frequencies that dominate the rate of sea level change record (Fig. S8). Good lagged correlations between RSL records and crustal thickness are observed, which align the large amplitude crustal thickness changes with the lowest frequency glacial cycles.

A quarter cycle time lag between sea level change and mantle melting response is expected, as well as further lags due to the time required for mantle melt perturbations to traverse the melting column, and the impacts of the finite width over which crust

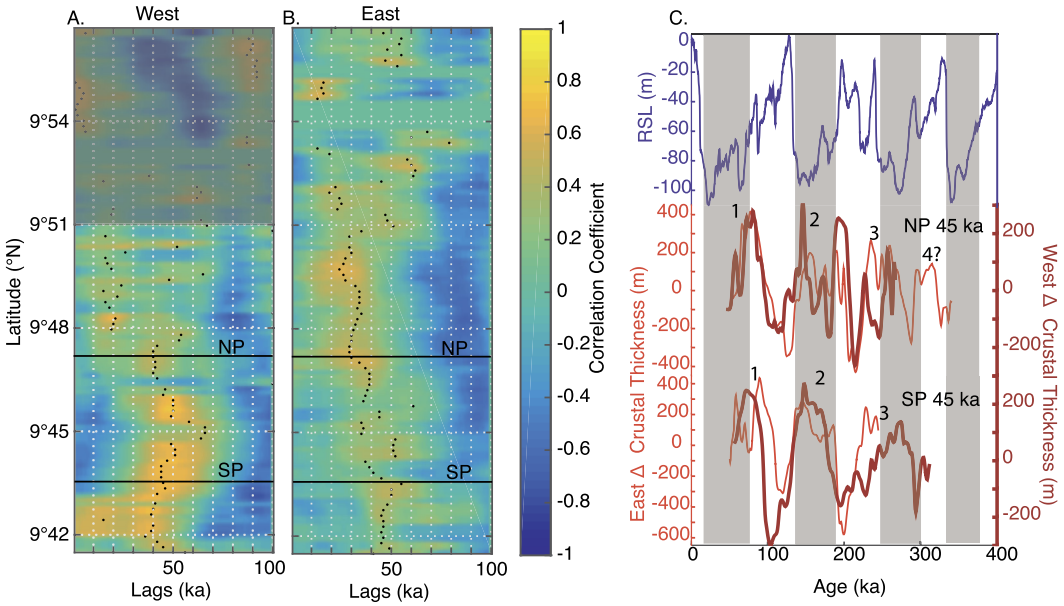

Fig. 8. Correlations between crustal thickness and relative sea level. Cross correlations are calculated between RSL (Grant et al., 2014) and crustal thickness on the west (A) and east (B) flanks, and plotted by lag time at latitude of profile intersection with the ridge axis, with color indicating correlation coefficient. Profiles were extracted from crustal thickness grids and filtered to frequencies between 1/10 ka^{-1} and 1/150 ka^{-1} prior to correlation calculation (see Methods, 4.1). Peak correlation for each profile is indicated with black dots. Correlations are calculated only in the direction of RSL change occurring prior to crustal thickness variation; hence lags are all positive Black lines indicate the location of two example profiles (northern profile-NP, southern profile-SP) shown in C. East (red) and west (maroon) flank profiles NP and SP, shifted by calculated lags (labeled) of best correlation compared with RSL (blue), with grey bars indicating glacial periods. Black numbers indicate crustal thickness ridges as in Fig. 1B.

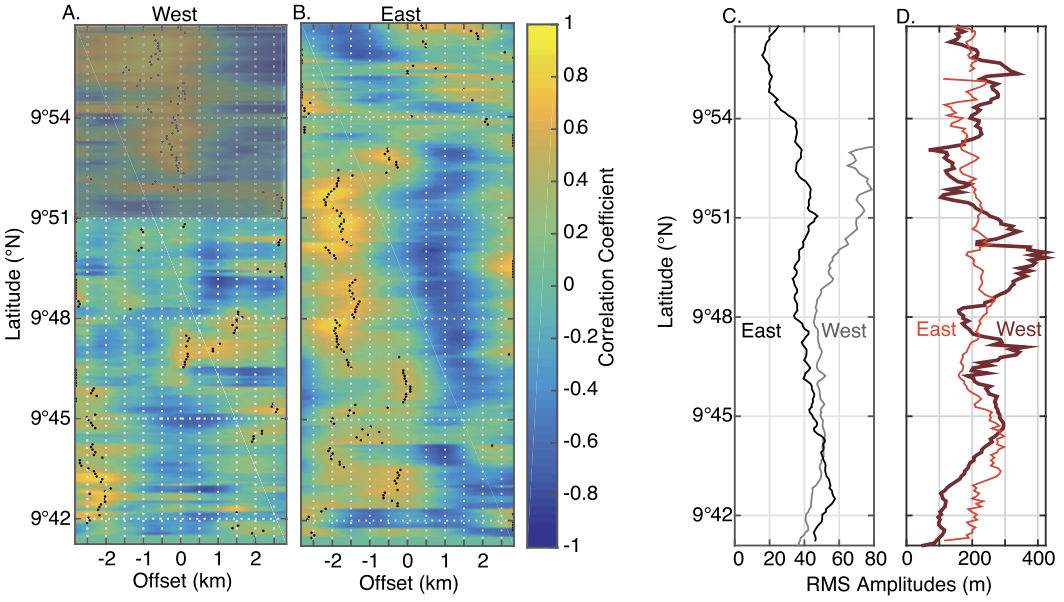

Fig. 9. Correlations between crustal thickness and bathymetry. Cross correlations are calculated between co-located crustal thickness and bathymetry profiles after filtering to frequencies between 1/75 m^{-1} and 1/7 km^{-1} to eliminate high frequency variations and any long term trends associated with seafloor subsidence (see Methods, 4.1). Correlations are shown for the west (A) and east (B) flanks, and plotted by offset in km and latitude of the ridge axis crossing of each profile, with color indicating correlation coefficient. Correlations are calculated with positive lags indicating crustal thickness profiles are shifted to further from the ridge axis. C. Calculated RMS amplitudes for bathymetry on the east flank (black) and west flank (grey). D. Calculated RMS amplitudes for crustal thickness on the east flank (red) and west flank (maroon).

is formed (e.g. Lund and Asimow, 2011; Crowley et al., 2015; Burley and Katz, 2015; Olive et al., 2015; Tolstoy, 2015). The ∼1.5 km (equivalent to ∼14 ka) wide zone of accretion centered at the ridge axis may account for part of the dominant lag of ∼45 ka between crustal thickness and RSL, implying a residual lag of ∼30 ka attributable to mantle melting response and melt ascent times. The presence and magnitude of a lag beyond that due to the width of the accretion zone has important implications for the sea level model. However, our crustal thickness dataset is short and observed correlations with RSL are modest. Future studies with longer crustal thickness time series and in other regions will be needed to further explore these implications.

5.2. Comparisons of spectral results for East and West flanks

Results of our spectral analysis indicate major differences between the east and west flanks that warrant further examination. While variations in bathymetry and crustal thickness on both flanks at similar long periodicities are evident from visual inspection, these similarities are less apparent in spectral analysis, par-

ticularly in bathymetry data. Spectrograms of east flank crustal thickness and bathymetry show evidence for a spectral peak centered at 1/80 ka^{-1} (Figs. 6A and 7A) and local regions with spectral peaks near 1/41 ka^{-1}. West flank crustal thickness spectral results also show regions of power centered at slightly lower frequencies of ~1/100 ka^{-1}, though less consistent than the east flank, and little coherent signal in spectral analysis of bathymetry (Fig. 6B and 7B). We attribute these results to differences in ridge flank structure due to the variable spreading asymmetry inferred for the region.

While conjugate bands of thicker crust are present on both ridge flanks, the TCR are not mirror image structures about the ridge but rather are mostly narrower, thinner and are more discontinuous features on the west flank than the east (Fig. 1B). Assuming the TCRs are coeval structures requires significant spreading asymmetry in the region, which has varied in sense and magnitude through time (Fig. 3B). Small (hundreds of meters to kilometer-scale) jumps in the locus of accretion within individual spreading segments likely transfer of crust from the west to the east, contributing to the narrower and more discontinuous TCRs on the west flank. As a result of their inconsistent and narrow width, the ~80-100 ka spaced TCR on the west flank would be expected to be more difficult to detect as a long-wavelength signal in spectral analysis (Fig. S9).

There are other geologic factors that may also contribute to differences in west and east flank structure including the off-axis volcanism associated with Sasha Seamount which has obscured 'normal' MOR topography and crustal thickness from the northern extent of our data to as far south as 9°50′N. The ridge flank discontinuity, which disrupts the thick crust ridges on both sides of the ridge axis, corresponds with a wider zone of thinner crust on the west flank and likely accounts for the diminished along-axis continuity of the TCR in this region. Overall however, we expect these factors to contribute less to differences in crustal spectra than the effects of the variable spreading asymmetry.

5.3. Seafloor relief as a record of crustal thickness variations

An important question arising from the recent studies of abyssal hill topography and the sea level hypothesis (Crowley et al., 2015; Tolstoy, 2015; Olive et al., 2015; Goff, 2015) is the nature of the relationship between seafloor relief and crustal thickness. In Crowley et al. (2015), the hypothesis that sea level variations result in changes in mantle melting and melt delivery to the crust is tested using seafloor bathymetry under the assumption that thicker crust is recorded in the bathymetric undulations of the seafloor through isostasy. For an Airy isostasy approximation, bathymetric variations that are 13-26% of crustal thickness variations are predicted for plausible crustal and mantle densities (Turcotte and Schubert, 2014).

Seafloor RMS amplitudes of 25-51 m are measured in our study, except in the vicinity of Sasha Seamount (Fig. 9C), similar to previously reported values, (Goff, 1991 – 34 ± 4 m to 56 ± 4 m) based on stochastic analysis of bathymetry in the region. These RMS amplitudes range from 10 to 29% of the observed RMS crustal thickness amplitudes, close to the percentages predicted for bathymetric relief due to isostatic compensation of crustal thickness.

Cross-correlations calculated between crustal thickness and bathymetry show good correlations at zero offset in parts of our study (Fig. 9A&B), as expected for direct isostatic compensation of seafloor topography. However, strong correlations at non-zero offsets are also found, with consistent patterns in the east flank dataset north of ~9°46.5′N. In this region, maximum correlations are at offsets of -1.75 km with the sense of offset indicating a shift of crustal thickness ridges closer to the MOR to best align with the seafloor ridges above.

We attribute the non-zero offsets to differences in the width of the crustal accretion zone in the upper and lower crust and misalignment in the locus of accretion linked to asymmetric spreading. Dike intrusion, which is the dominant process in the formation of the upper crust, is believed to be narrowly focused within the few 100 m wide axial summit trough that bisects the shallow ridge axis high (e.g. Fornari et al., 1998). The crustal thickness dataset shows a wider region (~1.5 km) of thin crust bounding the ridge axis (Fig. 1B), consistent with (albeit narrower than) the wider zone of distributed melt and high temperatures in the lower crust inferred from seismic tomography studies in the region (Dunn et al., 2000; Canales et al., 2012). Provided the loci of accretion in the upper and lower crust are aligned, periods of increased crustal production should result in collocated seafloor ridges and thick crust zones. However, small ridge jumps with misalignment of the locus of accretion in the upper and lower crustal could lead to offset bathymetry and crustal thickness ridges transported to the ridge flanks. The change from dominant offsets in the east flank data from near 0 to -1.75 km north of 9°46.5′N coincides with the observed ridge segmentation and is plausibly linked to small ridge jumps that have transferred crust to the east during asymmetric spreading in this region.

Complexity in the relationship between bathymetry and crustal thickness is also evident in the differences in spectral signatures of the two parameters across the study region. Bathymetry spectrograms show more power at higher frequencies than crustal thickness records, which likely reflects both higher resolution imaging in bathymetry records compared to crustal thickness as well as the effect of faulting which dominates seafloor relief and is largely confined to the upper crust. Average fault spacing in the area measured from a comprehensive regional mapping study is 0.9 km ± 0.1 km (Carbotte and Macdonald, 1994) and similar results are obtained using a subset of bathymetry data from our study (Fig. S10). Based on these observations we can attribute the diffuse spectral energy in bathymetry between 1/14 ka^{-1} and 1/20 ka^{-1} (equivalent to ~750 m – 1 km) to the dominant fault spacing (Fig. 7). The weak ~1/41 ka^{-1} signal apparent in bathymetry in the southern half of the east flank is consistent with the characteristic abyssal hill spacing measured in this region from prior analysis (Goff, 1991, average of ~2.0 km) and likely reflects the spacing of the larger amplitude longer-lived faults (Olive et al., 2015). It is important to note, however, that faulting and variations in crustal magma supply may be closely linked (e.g. via crustal thermal structure, impact on crustal stress state). The presence of an intermittent 1/41 ka^{-1} signal in our crustal thickness data does not rule out magmatic variability on these length scales. Recent fault modeling studies show faulting driven by sea level modulated magma supply at the 41 ka periodicities (Huybers et al., 2019).

6. Conclusions

High-resolution crustal imaging of a 25 km long region of the EPR extending to crustal ages of ~235 ka reveals three prominent ridge-parallel zones of 200-800 m thicker crust implying temporally variable crustal production in this region on ~80 ka time scales. Spectral analysis indicates peak frequencies near 1/80 to 1/100 ka^{-1}, consistent with visual observations, as well as near 1/41 ka^{-1} in parts of the region. Both the amplitude and wavelengths of the crustal thickness fluctuations are consistent with models of mantle melting in response to sea level variations of the Pleistocene. Cross-correlations between crustal thickness and RSL indicate maximum correlation at lags of ~45 ka, which aligns the thick crust zones with periods of lower sea level. While other processes could contribute to the fluctuations in crustal thickness observed in the region, glacially modulated mantle melting provides a plausible mechanism. Future high-resolution studies of crustal

thickness that sample longer crustal ages and using modern longer offset streamers, providing further improvements in crustal velocity estimation, in other regions will be needed to further test the hypothesis.

The availability of coincident high-resolution crustal thickness and bathymetry data provides the opportunity to examine the relationship between these two crustal properties and to address the question of if, and how, crustal thickness variations are recorded in bathymetry. Spectral analysis indicates similar spatial variations and similar longer wavelength peak frequencies in both datasets. The relative scales of seafloor and crustal thickness relief support a component of compensated topography. However, the data also indicate that the relationship between the two crustal properties is complicated. Cross-correlations between bathymetry and crustal thickness show strong correlations in parts of the study area at non-zero offsets, which could reflect the different widths of the upper and lower crustal accretion zone and misaligned locus of accretion during the variable asymmetric spreading and related ridge jumps inferred for the region. Spectral analysis shows more power overall, though diffuse, at higher frequencies in bathymetry data, which we attribute to the effects of data resolution and ridge-flank faulting. From the combined observations we infer that bathymetry and crustal thickness variations are linked, but that the effects of faulting, asymmetric spreading and the variable width accretion zone complicate the record.

Declaration of competing interest

The authors declare that they have no known competing financial interests or personal relationships that could have appeared to influence the work reported in this paper.

Acknowledgements

We thank John Goff, Jean-Arthur Olive, Jerry McManus, Kassandra Costa, Jennifer Middleton, Parker Liautaud, and Richard Katz for helpful discussions as well as David Lund and another anonymous reviewer for their thoughtful reviews, which greatly improved the manuscript. Support provided by NSF FESD Program Award AGS-1338832 to CL, SMC, PH.

Appendix A. Supplementary material

Supplementary material related to this article can be found online at https://doi.org/10.1016/j.epsl.2020.116121.

References

Aghaei, O., 2013. The East Pacific Rise Crustal Thickness, Moho Transition Zone Character and Off-Axis Magma Lens Melt Content From 9°37.5′N to 9°57′N: Results from Three-Dimensional Multi Channel Seismic Data Analysis. Dalhousie University.

Aghaei, O., et al., 2014. Crustal thickness and Moho character of the fast-spreading East Pacific Rise from 9°42′N to 9°57′N from poststack-migrated 3-D MCS data. Geochem. Geophys. Geosyst. 15 (3), 634–657.

Barth, G., Mutter, J., 1996. Variability in oceanic crustal thickness and structure: multichannel seismic reflection results from the northern East Pacific Rise. J. Geophys. Res., Solid Earth 101 (B8), 17951–17975.

Batiza, R., et al., 1996. Steady and non-steady state magma chambers below the East Pacific Rise. Geophys. Res. Lett. 23 (3), 221–224.

Buck, W.R., et al., 2005. Modes of faulting at mid-ocean ridges. Nature 434 (7034), 719.

Burley, J.M., Katz, R.F., 2015. Variations in mid-ocean ridge CO_2 emissions driven by glacial cycles. Earth Planet. Sci. Lett. 426, 246–258.

Canales, J., et al., 2003. Segment-scale variations in the crustal structure of 150–300 kyr old fast spreading oceanic crust (East Pacific Rise, 8°15′N–10°5′N) from wide-angle seismic refraction profiles. Geophys. J. Int. 152 (3), 766–794.

Canales, J., et al., 2012. Network of off-axis melt bodies at the East Pacific Rise. Nat. Geosci. 5 (4), 279.

Carbotte, S., Macdonald, K., 1992. East Pacific Rise 8°–10°30′N: evolution of ridge segments and discontinuities from SeaMARC II and three-dimensional magnetic studies. J. Geophys. Res., Solid Earth 97 (B5), 6959–6982.

Carbotte, S.M., Macdonald, K.C., 1994. Comparison of seafloor tectonic fabric at intermediate, fast, and super fast spreading ridges: influence of spreading rate, plate motions, and ridge segmentation on fault patterns. J. Geophys. Res., Solid Earth 99 (B7), 13609–13631.

Carbotte, S.M., et al., 2013. Fine-scale segmentation of the crustal magma reservoir beneath the East Pacific Rise. Nat. Geosci. 6 (10), 866.

Cerpa, N.G., Jones, D.W.R., Katz, R.F., 2019. Consequences of glacial cycles for magmatism and carbon transport at mid-ocean ridges. Preprint. arXiv:1904.03154.

Costa, K.M., et al., 2017. Hydrothermal deposition on the Juan de Fuca Ridge over multiple glacial–interglacial cycles. Earth Planet. Sci. Lett. 479, 120–132.

Crowley, J.W., et al., 2015. Glacial cycles drive variations in the production of oceanic crust. Science 347 (6227), 1237–1240.

Dunn, R.A., et al., 2000. Three-dimensional seismic structure and physical properties of the crust and shallow mantle beneath the East Pacific Rise at 9°30′N. J. Geophys. Res., Solid Earth 105 (B10), 23537–23555.

Fornari, D.J., et al., 1998. Axial summit trough of the East Pacific Rice 9°–10° N: geological characteristics and evolution of the axial zone on fast spreading mid-ocean ridge. J. Geophys. Res., Solid Earth 103 (B5), 9827–9855.

Goff, J.A., 1991. A global and regional stochastic analysis of near-ridge abyssal hill morphology. J. Geophys. Res., Solid Earth 96 (B13), 21713–21737.

Goff, J.A., 2015. Comment on "Glacial cycles drive variations in the production of oceanic crust". Science 349 (6252), 1065.

Goff, J.A., Jordan, T.H., 1988. Stochastic modeling of seafloor morphology: inversion of sea beam data for second-order statistics. J. Geophys. Res., Solid Earth 93 (B11), 13589–13608.

Goff, J.A., et al., 2018. No evidence for milankovitch cycle influence on abyssal hills at intermediate, fast, and superfast spreading rates. Geophys. Res. Lett.

Grant, K., et al., 2014. Sea-level variability over five glacial cycles. Nat. Commun. 5, 5076.

Haymon, R.M., et al., 1991. Hydrothermal vent distribution along the East Pacific Rise crest (9°09′–54′N) and its relationship to magmatic and tectonic processes on fast-spreading mid-ocean ridges. Earth Planet. Sci. Lett. 104 (2–4), 513–534.

Haymon, R.M., White, S.M., 2004. Fine-scale segmentation of volcanic/hydrothermal systems along fast-spreading ridge crests. Earth Planet. Sci. Lett. 226 (3–4), 367–382.

Huybers, P., et al., 2019. Abyssal hill faults paced by late-Pleistocene variations in sea level. In: 2019 Fall Meeting. AGU, San Francisco, CA.

Huybers, P., Langmuir, C., 2009. Feedback between deglaciation, volcanism, and atmospheric CO_2. Earth Planet. Sci. Lett. 286 (3–4), 479–491.

Huybers, P., Langmuir, C.H., 2017. Delayed CO_2 emissions from mid-ocean ridge volcanism as a possible cause of late-Pleistocene glacial cycles. Earth Planet. Sci. Lett. 457, 238–249.

Huybers, P., Wunsch, C., 2004. A depth-derived Pleistocene age model: uncertainty estimates, sedimentation variability, and nonlinear climate change. Paleoceanography 19 (1).

Kappel, E.S., Ryan, W.B., 1986. Volcanic episodicity and a non-steady state rift valley along northeast Pacific spreading centers: evidence from sea MARC I. J. Geophys. Res., Solid Earth 91 (B14), 13925–13940.

Lund, D.C., Asimow, P.D., 2011. Does sea level influence mid-ocean ridge magmatism on Milankovitch timescales? Geochem. Geophys. Geosyst. 12 (12).

Lund, D., et al., 2016. Enhanced East Pacific Rise hydrothermal activity during the last two glacial terminations. Science 351 (6272), 478–482.

Lund, D.C., Seeley, E.I., Asimow, P.D., Lewis, M.J., McCart, S.E., Mudahy, A.A., 2018. Anomalous Pacific Antarctic ridge volcanism precedes glacial termination 2. Geochem. Geophys. Geosyst. 19 (8), 2478–2491.

Macdonald, K.C., 1982. Mid-ocean ridges: fine scale tectonic, volcanic and hydrothermal processes within the plate boundary zone. Annu. Rev. Earth Planet. Sci. 10 (1), 155–190.

Macdonald, K.C., et al., 1996. Volcanic growth faults and the origin of Pacific abyssal hills. Nature 380 (6570), 125–129.

Macdonald, K.C., 1998. Linkages between faulting, volcanism, hydrothermal activity and segmentation on fast spreading centers. In: Faulting and Magmatism at Mid-Ocean Ridges, pp. 27–58.

Marjanović, M., et al., 2018. Crustal magmatic system beneath the East Pacific Rise (8°20′ to 10°10′N): implications for tectonomagmatic segmentation and crustal melt transport at fast-spreading ridges. Geochem. Geophys. Geosyst. 19 (11), 4584–4611.

Middleton, J.L., et al., 2016. Hydrothermal iron flux variability following rapid sea level changes. Geophys. Res. Lett. 43 (8), 3848–3856.

Olive, J.-A., et al., 2015. Sensitivity of seafloor bathymetry to climate-driven fluctuations in mid-ocean ridge magma supply. Science 350 (6258), 310–313.

Parsons, B., Sclater, J.G., 1977. An analysis of the variation of ocean floor bathymetry and heat flow with age. J. Geophys. Res. 82 (5), 803–827.

Percival, D.B., Walden, A.T., 1993. Spectral Analysis for Physical Applications. Cambridge University Press.

Raymo, M.E., 1997. The timing of major climate terminations. Paleoceanography 12 (4), 577–585.

Regelous, M., et al., 1999. Variations in the geochemistry of magmatism on the East Pacific Rise at 10°30′N since 800 ka. Earth Planet. Sci. Lett. 168 (1–2), 45–63.
Sims, K., et al., 2003. Aberrant youth: chemical and isotopic constraints on the origin of off-axis lavas from the East Pacific Rise, 9°–10°N. Geochem. Geophys. Geosyst. 4 (10).
Soule, S.A., et al., 2007. New insights into mid-ocean ridge volcanic processes from the 2005–2006 eruption of the East Pacific Rise, 9°46′N–9°56′N. Geology 35 (12), 1079–1082.
Tolstoy, M., 2015. Mid-ocean ridge eruptions as a climate valve. Geophys. Res. Lett. 42 (5), 1346–1351.
Toomey, D.R., et al., 2007. Skew of mantle upwelling beneath the East Pacific Rise governs segmentation. Nature 446 (7134), 409.
Turcotte, D., Schubert, G., 2014. Geodynamics. Cambridge University Press.
Tushingham, A., Peltier, W., 1991. Ice-3G: a new global model of late Pleistocene deglaciation based upon geophysical predictions of post-glacial relative sea level change. J. Geophys. Res., Solid Earth 96 (B3), 4497–4523.
White, S.M., et al., 2002. Correlation between volcanic and tectonic segmentation of fast-spreading ridges: evidence from volcanic structures and lava flow morphology on the East Pacific Rise at 9°–10°N. J. Geophys. Res., Solid Earth 107 (B8), EPM 7-1-EPM 7-20.
White, S.M., et al., 2006. A new view of ridge segmentation and near-axis volcanism at the East Pacific Rise, 8°–12°N, from EM300 multibeam bathymetry. Geochem. Geophys. Geosyst. 7 (12).